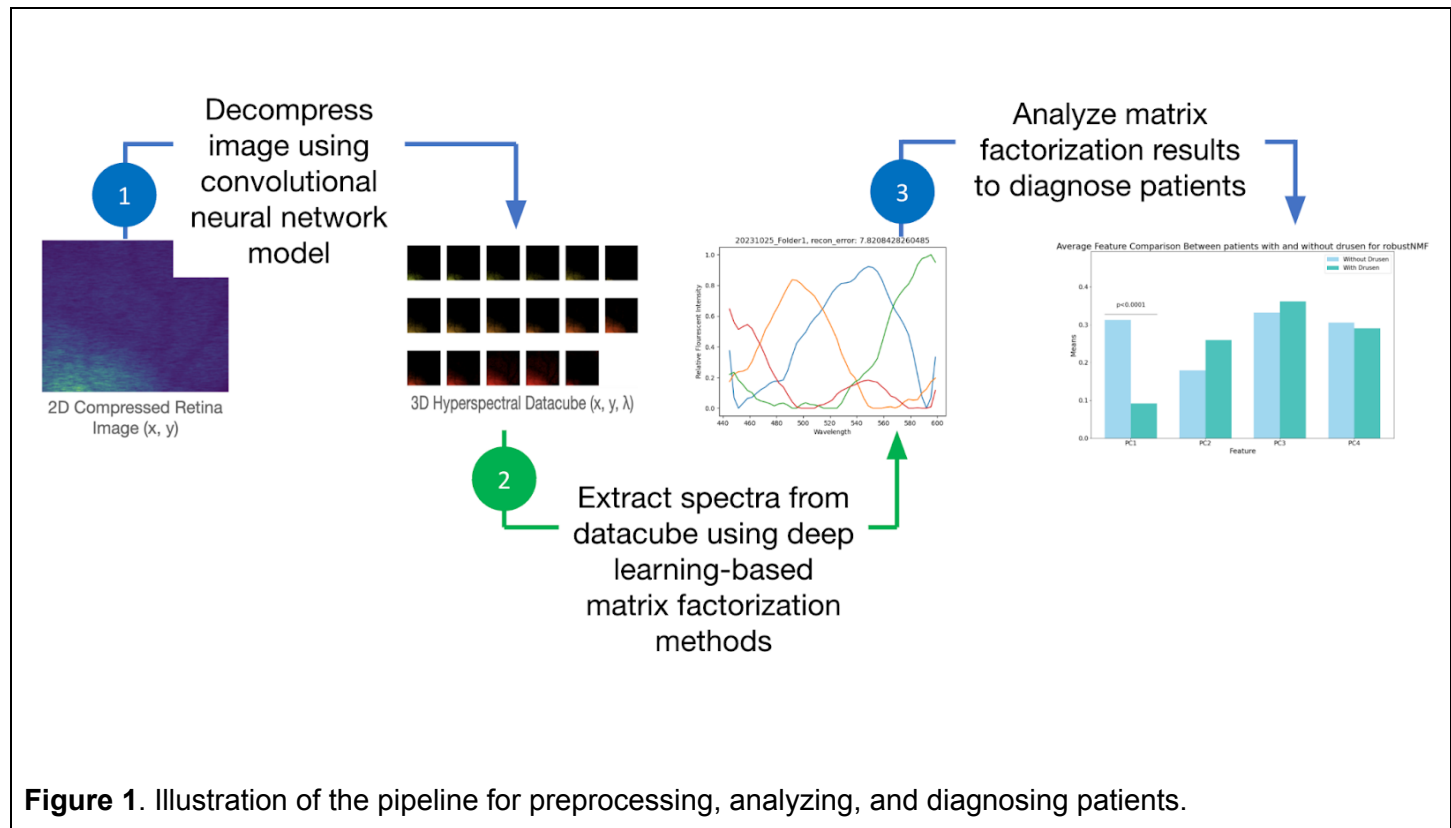
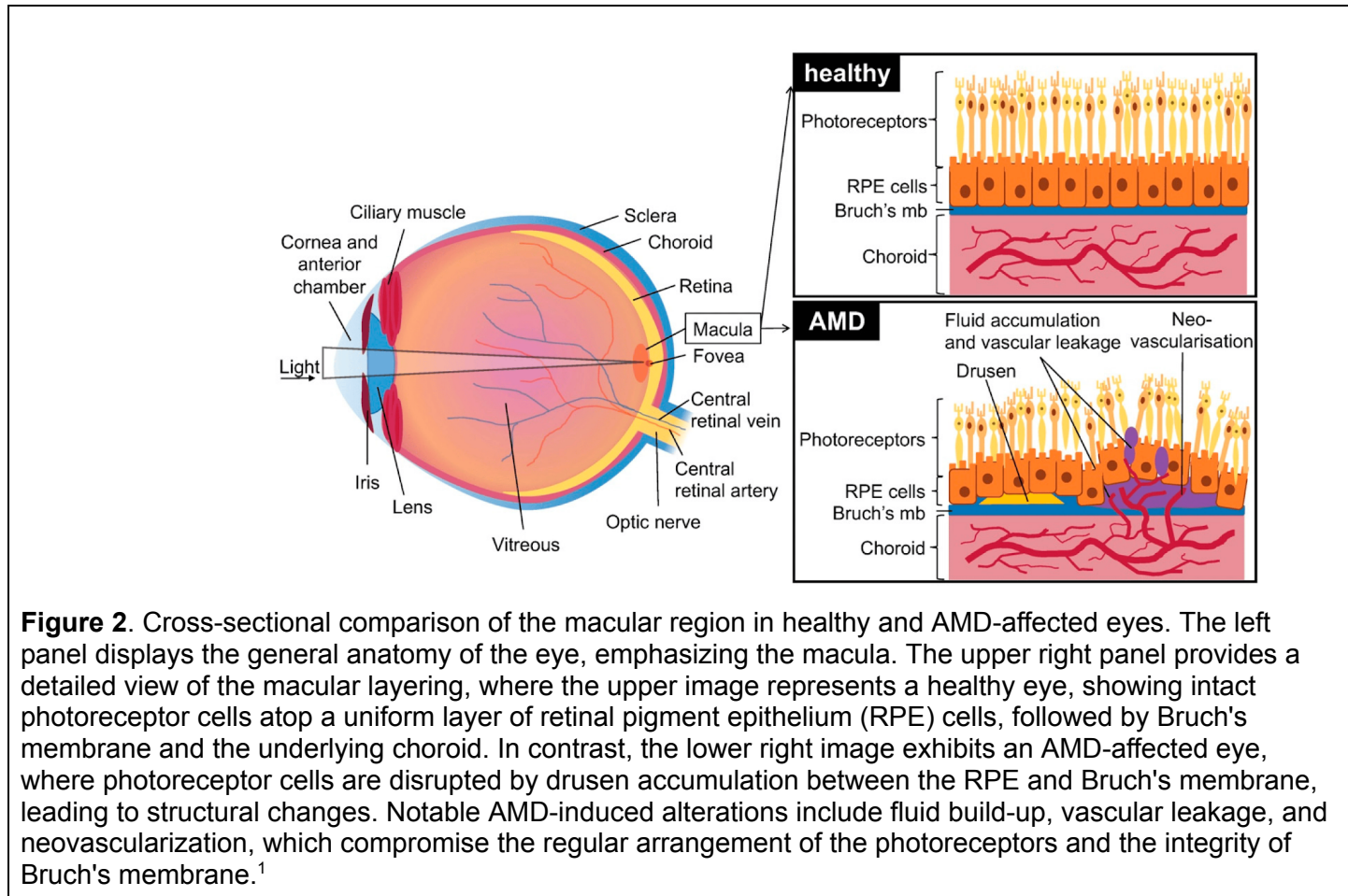


**Abstract:** In the expanding field of medical diagnostics, hyperspectral imaging (HSI) emerges as a pivotal innovation, particularly for its potential in the early detection and monitoring of drusen lesions, which are small spots on the retina associated with Age-related Macular Degeneration (AMD).<sup>1</sup> Current methods for reconstructing hyperspectral images of the eye and extracting spectral signatures from these images for diagnosis face challenges related to efficiency and applicability to *in vivo* data. This study lays the groundwork for future research to refine these techniques and expand their application within clinical settings. Our project addresses these challenges by proposing a novel solution leveraging deep learning techniques to enhance image reconstruction and diagnostic algorithms. The process begins with the decompression of a 2D compressed retina image using a convolutional neural network model, resulting in a 3D hyperspectral datacube. Subsequently, emission spectra of the eye are extracted from this datacube employing a deep learning-based matrix factorization method called Elastic Adversarial Deep Nonnegative Matrix Factorization (EADNMF).<sup>15</sup> The matrix factorization results are analyzed to identify patients at risk for AMD, distinguishing between subjects with and without drusen based on average principal component (PC) scores obtained through the EADNMF technique; a schematic diagram of the process described can be seen in Figure 1. Our findings suggest that deep learning methods show improved computational efficiency compared to traditional methods for HSI reconstruction and extraction of spectral signatures from an HSI, thereby offering promising prospects for improving *in vivo* AMD detection.



**Introduction:** AMD is a prevalent cause of vision loss, affecting millions of people worldwide. This condition primarily affects the Bruch's membrane and rod photoreceptor cells in the macula, the central part of the retina, resulting in blurred or absent vision in the center of the visual field. Early detection of AMD is crucial as there is currently no cure, and lifestyle changes are the only effective way to slow its progression.<sup>1</sup> Figure 2 demonstrates the difference between healthy and affected retinas.



**Figure 2.** Cross-sectional comparison of the macular region in healthy and AMD-affected eyes. The left panel displays the general anatomy of the eye, emphasizing the macula. The upper right panel provides a detailed view of the macular layering, where the upper image represents a healthy eye, showing intact photoreceptor cells atop a uniform layer of retinal pigment epithelium (RPE) cells, followed by Bruch's membrane and the underlying choroid. In contrast, the lower right image exhibits an AMD-affected eye, where photoreceptor cells are disrupted by drusen accumulation between the RPE and Bruch's membrane, leading to structural changes. Notable AMD-induced alterations include fluid build-up, vascular leakage, and neovascularization, which compromise the regular arrangement of the photoreceptors and the integrity of Bruch's membrane.<sup>1</sup>

Traditionally, the Amsler grid, a diagnostic tool consisting of a grid of evenly spaced horizontal and vertical lines, has been a fundamental tool for detecting signs of AMD. However, its effectiveness is limited due to its subjective nature, relying on patients' reports of distortions or blurriness in the grid pattern. Moreover, it often identifies AMD at a later stage, when significant damage may have already occurred, making early intervention more challenging.<sup>2</sup> Nevertheless, advancements in imaging techniques have enabled a more objective and comprehensive assessment of the retina. Imaging methods like optical coherence tomography (OCT) and fundus photography have emerged, yet they exhibit limitations in detecting early biochemical changes that indicate AMD.<sup>3,4</sup>

To address the limitations of standard Red, Green, and Blue (RGB) imaging in identifying subtle retinal changes linked to AMD, hyperspectral imaging (HSI) presents a notable improvement. HSI captures a wide range of wavelengths by utilizing a specialized sensor that splits light into many narrow bands. Specifically, the narrow bands of light enable the generation of emission spectra. This detailed spectral information is essential for identifying specific biochemical compounds present in the eye with unique light absorption properties, such as drusen, a characteristic deposit present in AMD; recognizing these changes is essential for early diagnosis.<sup>5</sup>

The Coded Aperture Snapshot Spectral Imaging (CASSI) system leverages HSI to rapidly capture images that reveal the intricate spectral signatures of these compounds.<sup>6</sup> This capability is particularly important in distinguishing healthy tissue from areas affected by drusen accumulation, a characteristic feature of AMD that alters the tissue's light absorption and scattering properties.

While fundus cameras provide a broad view of the retina for assessing its overall condition, they cannot provide the spectral information necessary to understand the biochemical changes associated with AMD. The CASSI system fills this gap by offering a detailed view of the retina's spectral response. The combination of fundus imaging and CASSI offers a comprehensive diagnostic evaluation for AMD, where fundus imaging provides a macroscopic view, and CASSI provides detailed microscopic spectral information, enhancing the overall assessment.<sup>7</sup>

The rapid acquisition of images in the CASSI system is accomplished by employing a coded aperture that applies a distinctive encoding to each wavelength before projecting it onto an image sensor. This design enables capturing a broad spectral range in a single snapshot, enhancing efficiency and significantly reducing data acquisition time. This quick capture capability is particularly beneficial in clinical settings where patient movement can compromise imaging quality.<sup>6,7</sup> Compared to traditional methods that require sequential scanning or lengthy exposure times, the CASSI system's approach is more suitable for dynamic and real-time applications.

Moreover, the advent of deep learning has brought about a transformative impact on the processing and examination of medical images. Specifically, convolutional neural networks (CNNs) are a category of powerful deep learning algorithms for visual analysis, and encoder-decoder models are a type of neural network architecture designed for data conversion tasks.<sup>8,9</sup> Current iterative methods for reconstructing hyperspectral images, such as Augmented Lagrangian (AL), take several hours and are therefore unideal for *in vivo* applications. Once trained, CNNs can generate HSIs with the immediacy necessary for patients. One caveat to training CNNs is their reliance on patient data, which presents significant challenges in sourcing, standardization, and patient privacy. However, self-supervised training loops can eliminate the need for large quantities of data and enable neural networks to provide fast and accurate reconstructions.

However, the application of HSI analysis presents a unique set of challenges when adapted to hyperspectral fluorescence microscopy. Hyperspectral fluorescence microscopy, unlike traditional HSI applications, involves the acquisition of high-dimensional data sets that capture both spatial and spectral information at a microscopic scale. This complexity demands advanced image processing and analysis techniques to effectively extract meaningful information. The high dimensionality of the data can lead to computational challenges, while the need to preserve the integrity of the delicate biological samples imposes constraints on the imaging process. Additionally, interpreting the spectral signatures in the context of biological structures is particularly challenging due to the complexity of biological spectra, which often involve mixing multiple components.<sup>10</sup> This complexity necessitates a deep understanding of the imaging technology and the biological systems under investigation to disentangle and analyze the underlying spectral information accurately.

Our project aims to develop an advanced algorithm with unprecedented computational efficiency for the *in vivo* diagnosis of AMD. By harnessing HSIs, we seek to detect the subtle yet significant changes within the retinal tissues associated with AMD. A key aspect of our approach involves the application of Elastic Adversarial Deep Nonnegative Matrix Factorization (EADNMF), a neural network model, to extract spectra from *in-vivo* patients (Figure 3). This represents an innovative advancement over the commonly used technique of Nonnegative Matrix Factorization (NMF), which separates images into components that reveal the underlying spectral signatures of the eye.<sup>11</sup> Our project focuses on refining algorithms for reconstructing HSI data and

innovating diagnostic algorithms. By leveraging deep learning, we enhance the computational efficiency of in vivo AMD detection, representing a significant advancement in managing this prevalent condition.

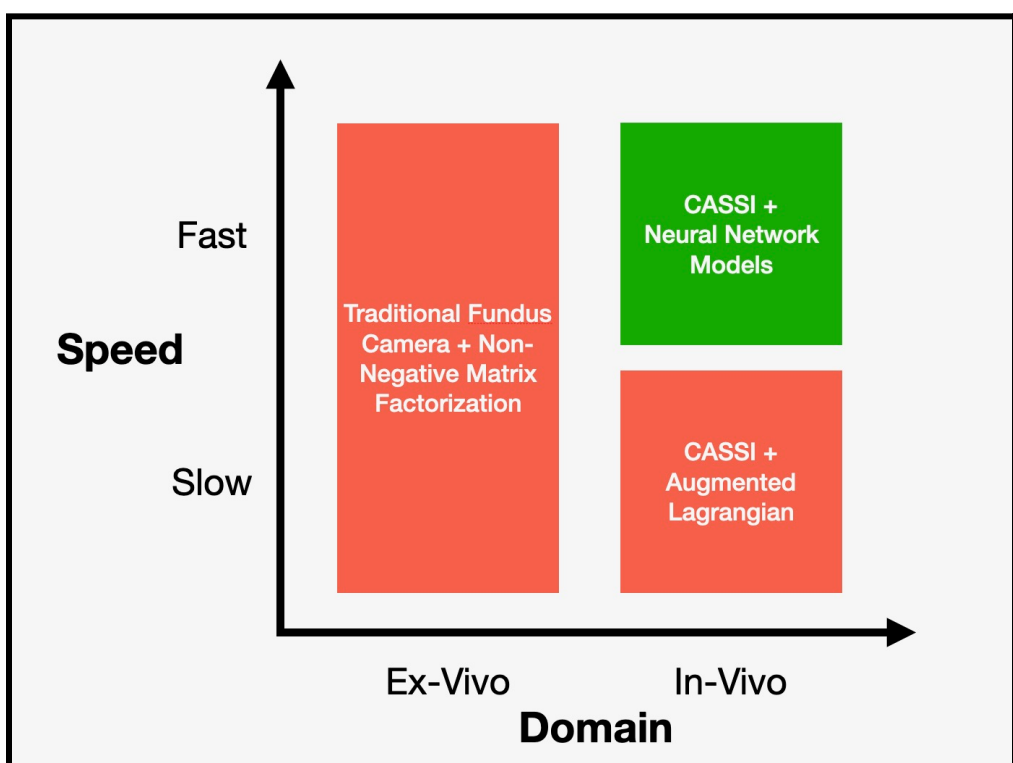


**Figure 3.** Diagnostic methods for AMD are categorized by speed and application domain. The method described in this paper is CASSI+Neural Network models (green).

## Methods:

### *Hyperspectral Image Reconstruction*

The original images taken by the fundus camera were reconstructed into HSIs using three combinations of convolutional neural network models and training algorithms. The first method used a basic U-Net model architecture consisting of several downsampling, upsampling, and residual layers (Figure 4). As shown in Figure 4, downsampling layers involve scaling down the x and y dimensions while scaling up the third  $\lambda$  dimension, and upsampling layers scale the x and y dimensions back up. Residual layers preserve the intermediate layers, allowing future layers to use them. The U-Net architecture is a standard for generative convolutional neural networks. Starting with a two-dimensional image of a retina as input, the model constructed a three-dimensional hypercube containing the x, y, and  $\lambda$  dimensions. The first model was trained using a standard supervised loop (Figure 5a), where a mean-squared error (MSE) loss was calculated between the true (Augmented Lagrangian) HSI and the model reconstructed HSI.

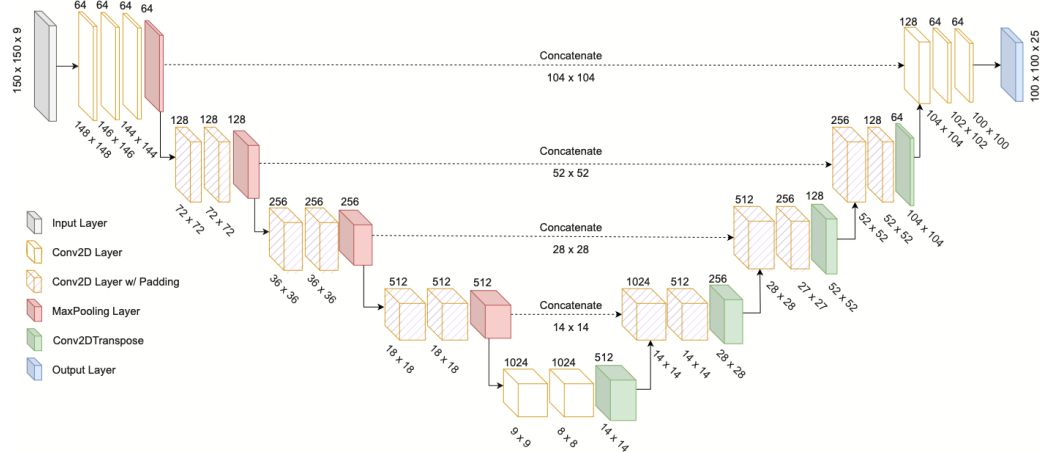


**Figure 4.** U-Net model architecture.<sup>18</sup>

The second method also used a U-Net architecture but with a self-supervised learning loop (Figure 5b), which addressed the problem of patient data scarcity. Under the self-supervised loop, the model reconstructed a 3D HSI from a 2D retina image as in the supervised method. Then, a function compressed the HSI back into a 2D retina in the same way that the fundus camera created a 2D retina image. Figure 6 illustrates the similarities between the camera-captured eye images and the eye images compressed from their respective HSIs. The output image was supposed to match the input image, so the training loop calculated the MSE loss between the input and output images to train the model. The self-supervised loop offered two advantages. First, because the model was trained to produce the same image as the input after compression, the model could use images other than the retina as the input, avoiding overfitting and reliance on limited patient data. Second, this structure did not require time-consuming Augmented Lagrangian reconstructions of retinas as labels for every data point. Our third method used the Deep Unfolding neural network model specifically designed for HSI reconstruction combined with the self-supervised training algorithm.<sup>7</sup>

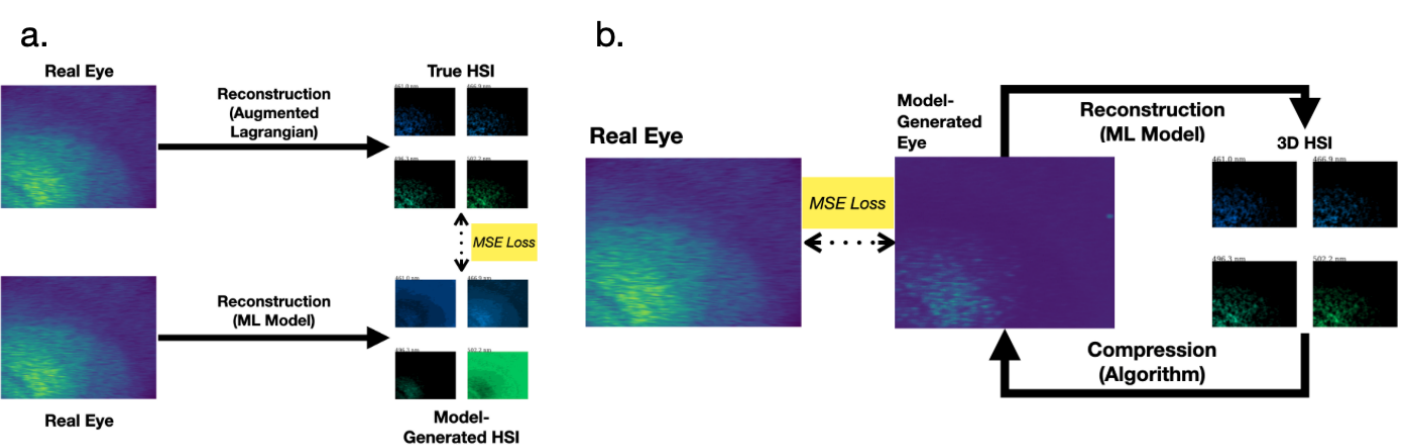


**Figure 5.** Training loop architectures. **a.** Supervised training loop. **b.** Self-supervised training loop (Bourdev 2024).

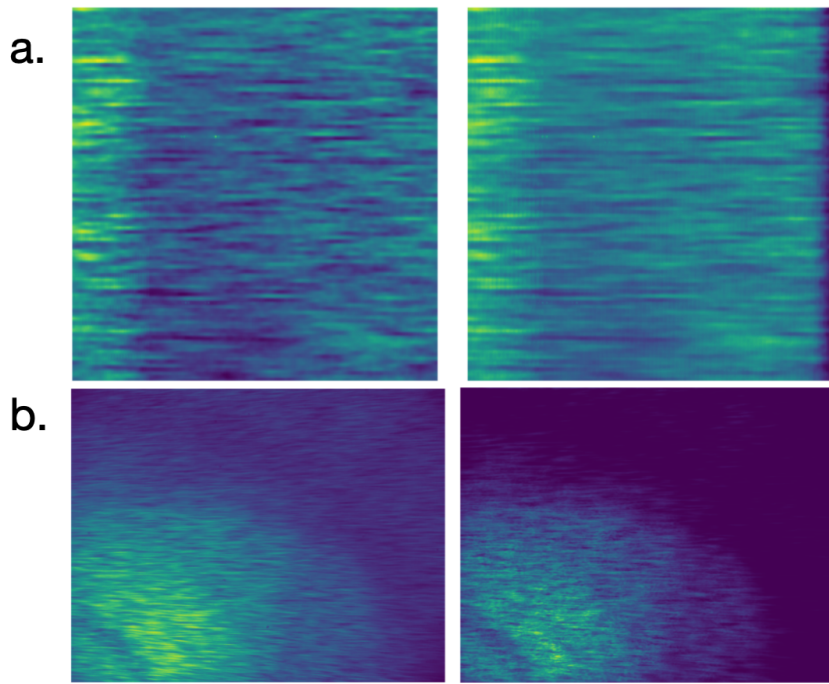


**Figure 6.** Comparison between retina images captured from fundus camera (left) and compressed from HSI (right). **a.** Retina images used by Deep Unfolding model. **b.** Retina images used by U-Net model.

We used several metrics to compare our self-supervised model approach with the current iterative Augmented Lagrangian approach, Deep Unfolding model, and diffusion model. We measured training time, model size, and training and validation losses.

#### Spectra Extraction

Next, we adapted an algorithm to process the HSIs of patient tissue *in vivo* and obtained the emission spectra, which improves our ability to identify drusen lesions for the diagnosis of patients with AMD.<sup>14</sup> We improved upon existing non-negative matrix factorization (NNMF) algorithms to analyze the HSIs. The hyperspectral data cubes must first undergo preprocessing to convert them to matrices. Matrices were constructed through mode-3 matricization of the hyperspectral data cubes for each patient.<sup>12</sup> Then, two algorithms for spectral extraction were adapted to analyze the HSIs using the Hoffman2 computing cluster in order to select the optimal algorithm. The iterative robust-NMF Python package for spectra extraction was selected because the algorithm works well for noisy data.<sup>15</sup> We ran the robust-NMF algorithm on the HSI matrices using the default parameters to obtain distinct spectral signatures and then adapted the parameters further to achieve more accurate results.

Iterative methods for extracting spectra from HSIs may not be as computationally efficient compared to deep learning methods due to limitations of scalability and parallelization. The EADNMF package provided a powerful tool for deep non-negative matrix factorization using a technique known as Elastic Adversarial Deep Nonnegative Matrix Factorization for Matrix Completion.<sup>16</sup> We applied the EADNMF algorithm with its default parameters to a complex matrix. EADNMF's integration of adversarial training within the model architecture sets it apart. This approach not only enhances the model's predictive accuracy in the presence of noisy data but also safeguards against overfitting tendencies.<sup>17</sup> EADNMF's ability to balance robustness and generalization allowed us to more efficiently extract the emission spectra.

Once the optimal parameters for the modified iterative NNMF and deep NNMF algorithms were selected, the spectra obtained were compared to determine if there was a significant difference between spectra extracted from the robust-NMF and deep learning algorithms. This allowed us to select the optimal method for HSI analysis for spectral extraction. The first step of spectral comparison involved normalizing the spectra to a unit 2-norm, a technique that effectively isolates shape changes for comparative analysis. Subsequently, we performed functional principal component analysis (fPCA) on the normalized spectra, employing the Bayesian Information Criterion to guide model selection and prevent overfitting. fPCA was used for dimensionality reduction and feature extraction to identify the dominant modes of variation. From this analysis, four principal eigenvalues were extracted, and corresponding sets of coefficients were obtained to represent the eigenbasis. The choice of four principal components was based on a trade-off between capturing sufficient variance in the data and maintaining a manageable dimensionality for subsequent analysis. To determine the significance of observed differences, statistical testing was utilized, specifically the Wilcoxon signed-rank test applied to pairs of coefficients. Additionally, a t-test was employed to conclude statistical significance, with a p-value threshold of less than 0.05 considered statistically significant. To mitigate the issue of multiple comparisons, p-values were adjusted using the Bonferroni correction, ensuring robustness in the statistical inference drawn from the data by reducing the rate of Type I errors. A similar process of spectral comparison was also applied to determine if there was a significant difference between spectra extracted from healthy patients compared to the spectra obtained from patients with AMD or drusen lesions.

## Results:

### Hyperspectral Image Reconstruction

We successfully built and trained our three models: supervised U-Net, self-supervised U-Net, and self-supervised Deep Unfolding network. We trained them each for 500 epochs using a learning rate of  $10^{-4}$ .

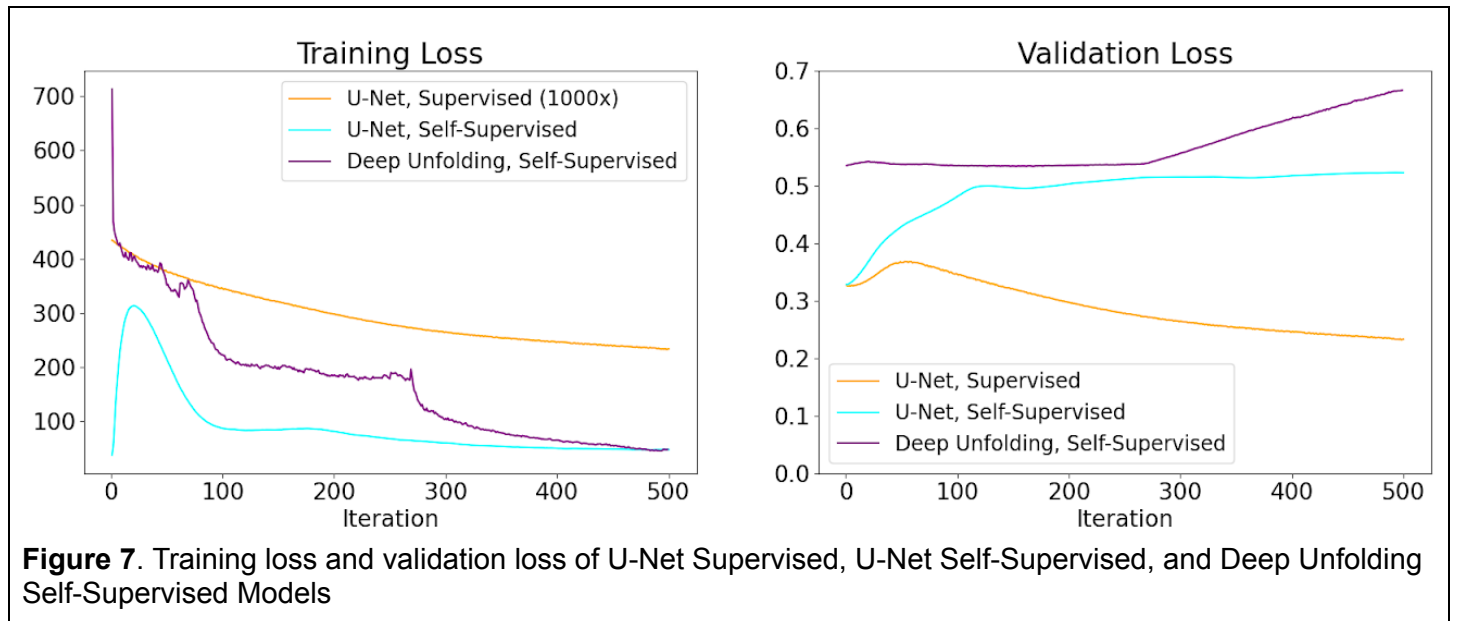
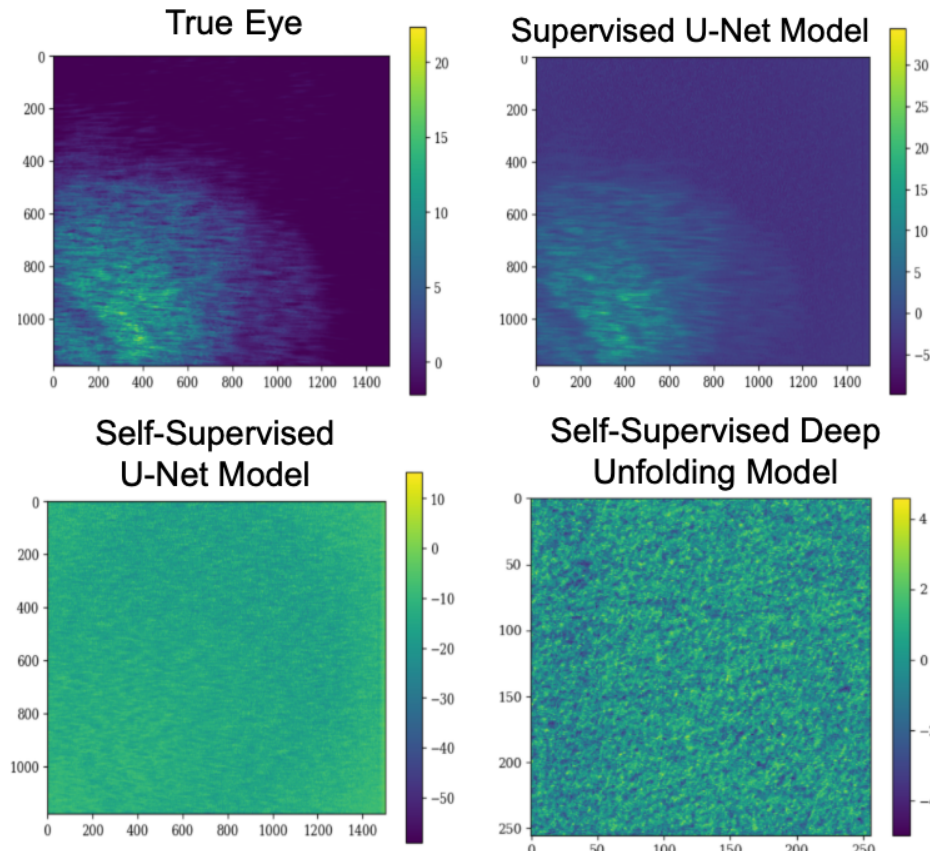


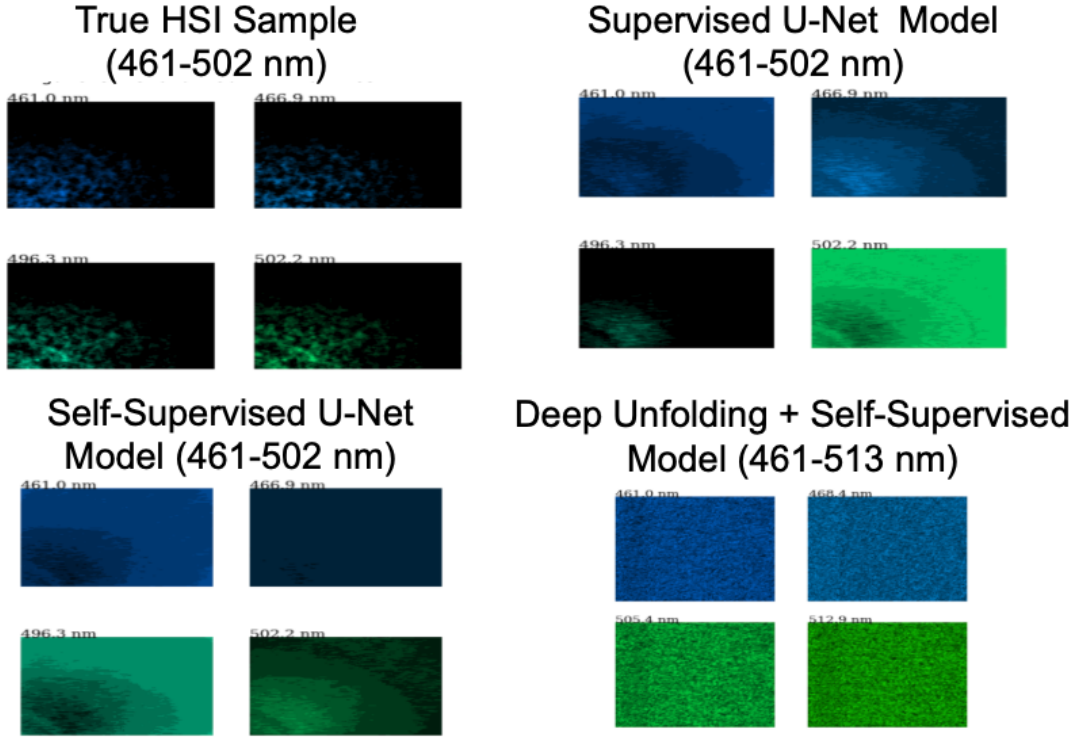
Figure 7 depicts the training and validation losses for each of the three model setups. The training losses for the self-supervised models are calculated between the input and output two-dimensional retina images. The training losses for the supervised model and all of the validation losses are calculated between the model-reconstructed three-dimensional HSI and the HSI produced by the iterative Augmented Lagrangian method.

All three models achieved a decrease in training loss as expected. However, none of the models demonstrate a significant decrease in validation loss, indicating that none of the models learned to produce HSIs similar to that of the Augmented Lagrangian method.



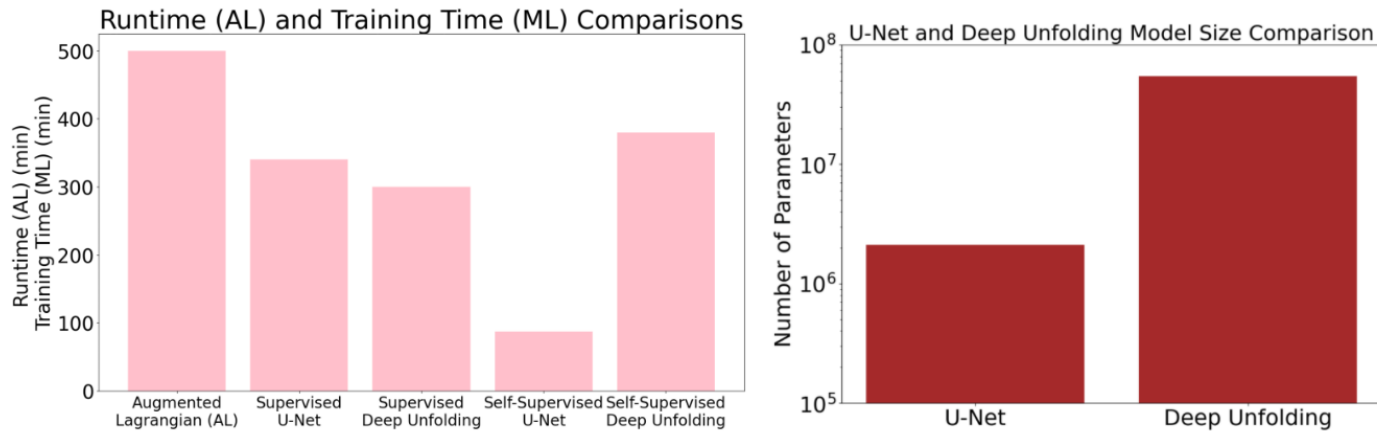
**Figure 8.** Image of an eye captured by a fundus camera (top left). Prediction of the image of an eye after 500 iterations of the supervised U-Net model (top right), self-supervised U-Net model (bottom left), and self-supervised Deep Unfolding model (bottom right).

Figure 8 depicts the retina image using the fundus camera compared to the retina image predictions produced by the three models, where the bars next to each picture depict the pixel values corresponding to those on the image. While each model achieves a reduction in training loss, only the supervised U-Net model produces a visually comparable eye image to the original.



**Figure 9.** Hyperspectral datacubes at wavelengths 461, 467, 496, and 502 nm produced from the Augmented Lagrangian algorithm (top). Predicted hyperspectral data cubes produced from the supervised U-Net model (top right), self-supervised U-Net model (bottom left), and self-supervised Deep Unfolding model (bottom right).

Figure 9 depicts four wavelengths of the three-dimensional HSIs produced by the Augmented Lagrangian algorithm compared to the three models. While in Figure 8, the supervised U-Net produced a visually comparable eye image, none of the models created HSIs comparable to that of the iterative algorithm. Interestingly, both U-Net models produce similar HSIs, but the HSIs are compressed into visually distinct eye images.

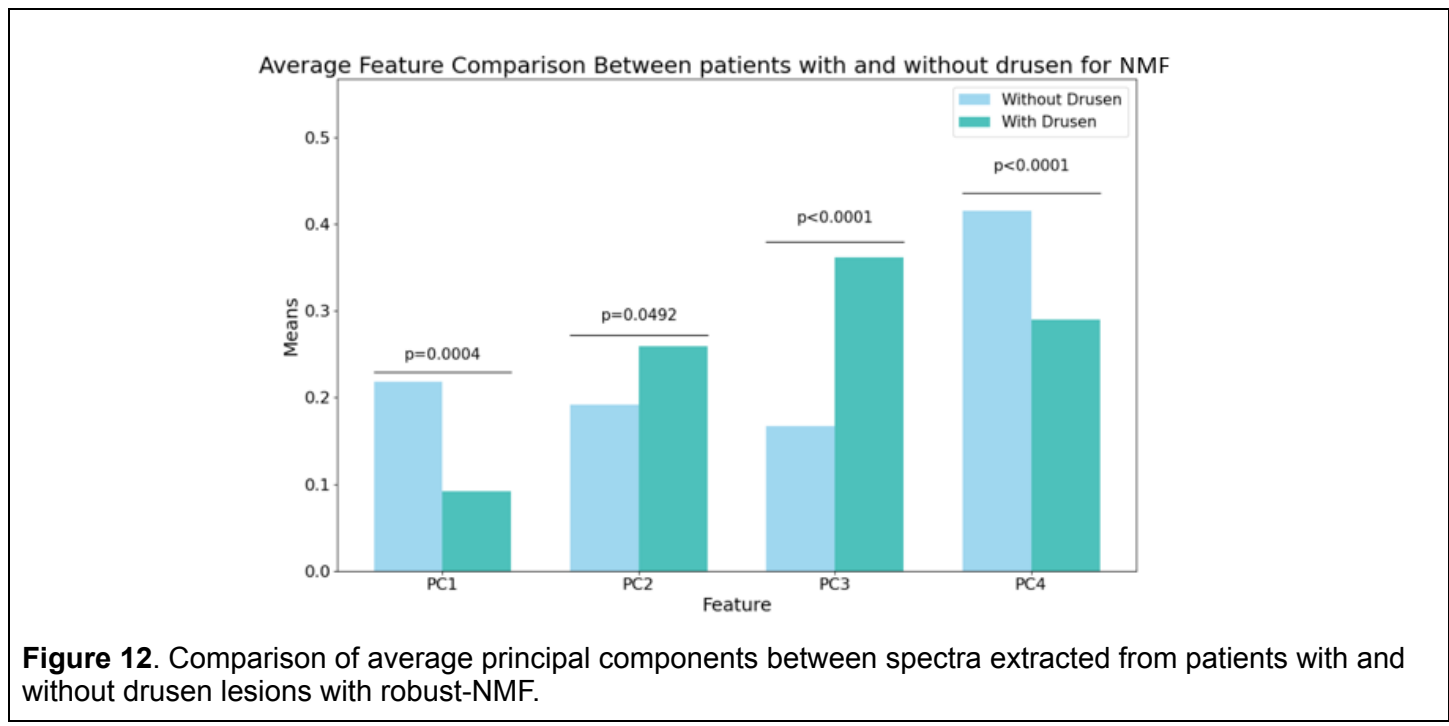
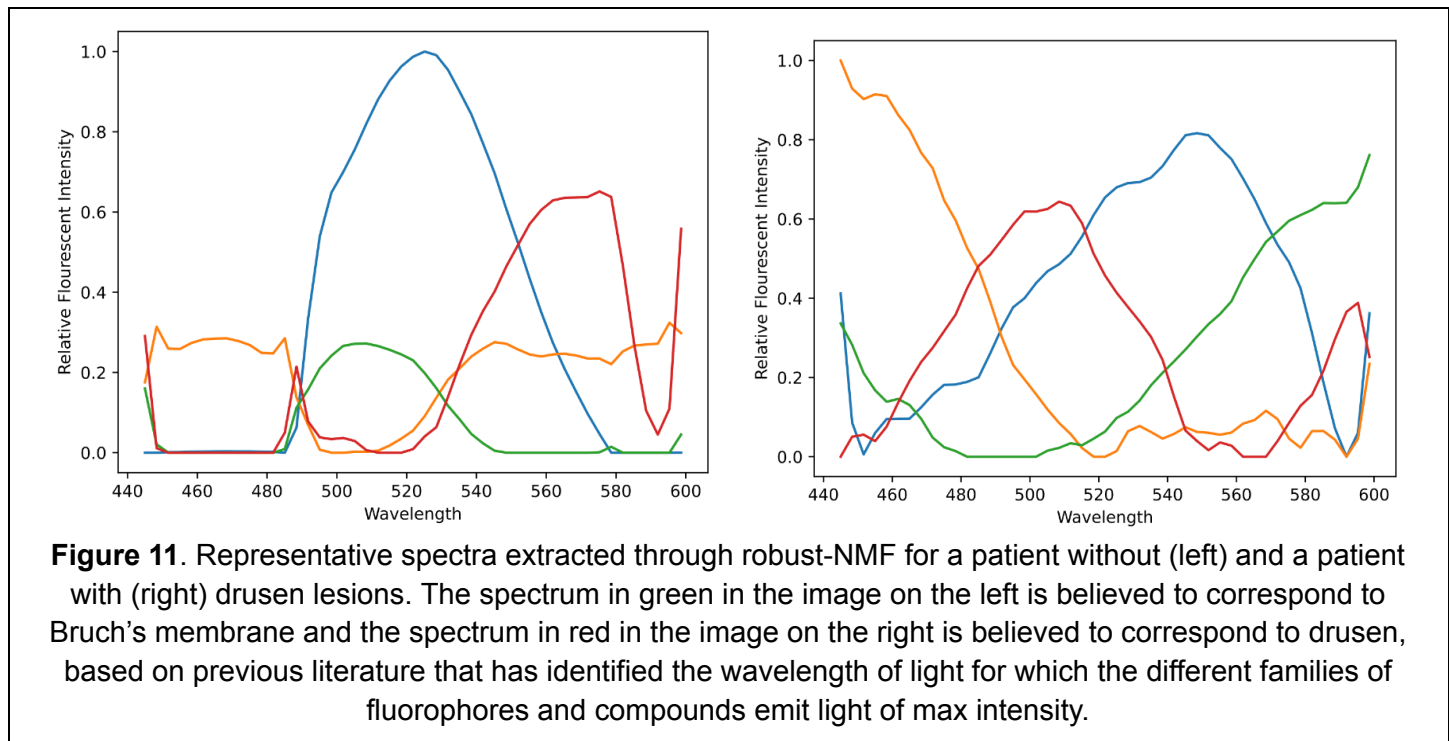


**Figure 10.** Comparison of AL model run and ML train times (left). Comparison of model sizes (right).

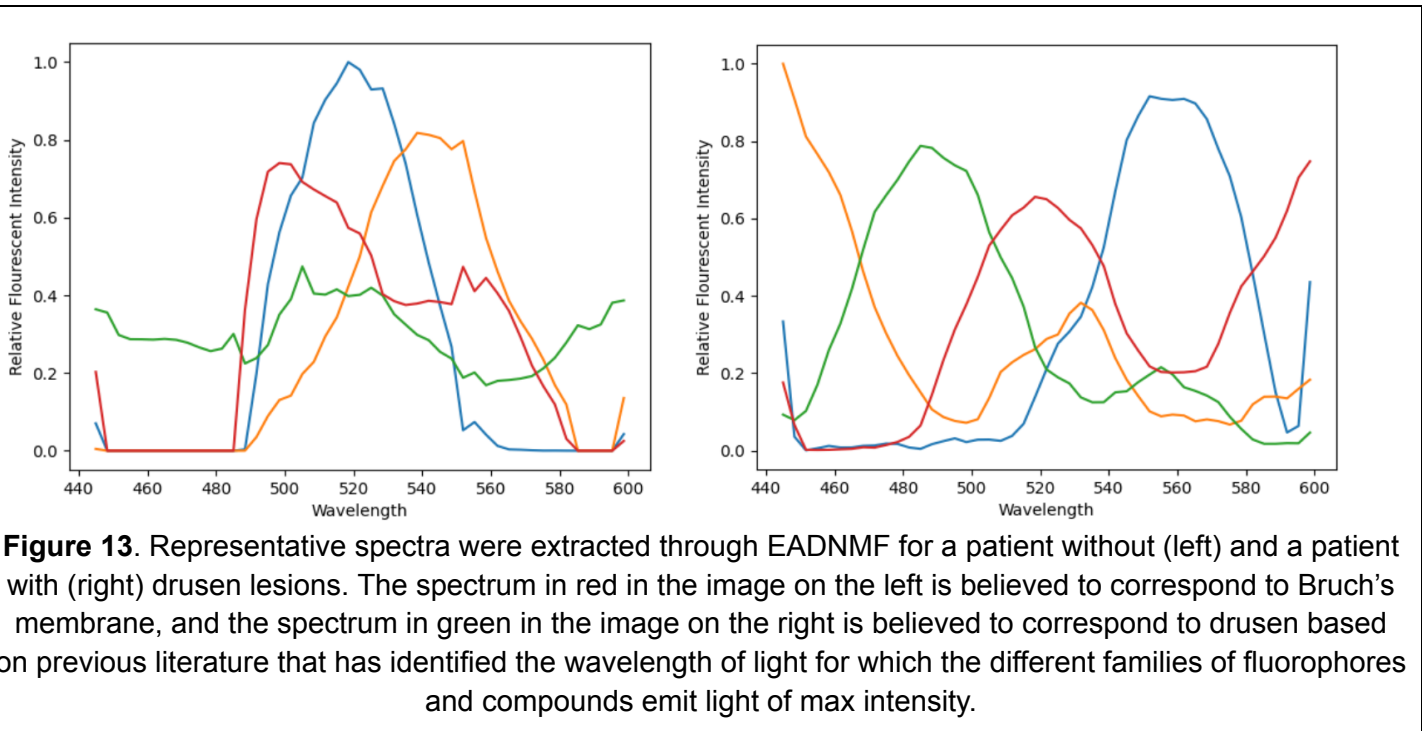
Figure 10 compares the quality of the models in terms of training time and size. After each model ran through 500 iterations, we found that all of the models produced training times that were shorter than the run time of

the iterative Augmented Lagrangian model, exhibiting the computational efficiency of the machine learning models that we implemented. Therefore, even if the model required training on a per-patient basis, it would still represent an improvement in runtime over the Augmented Lagrangian algorithm. The self-supervised U-Net model achieves the fastest training time for 500 iterations at about one and a half hours. As for the model size comparison, we found that the U-Net architecture only required 1/25th of the number of parameters that were used by the Deep Unfolding model.

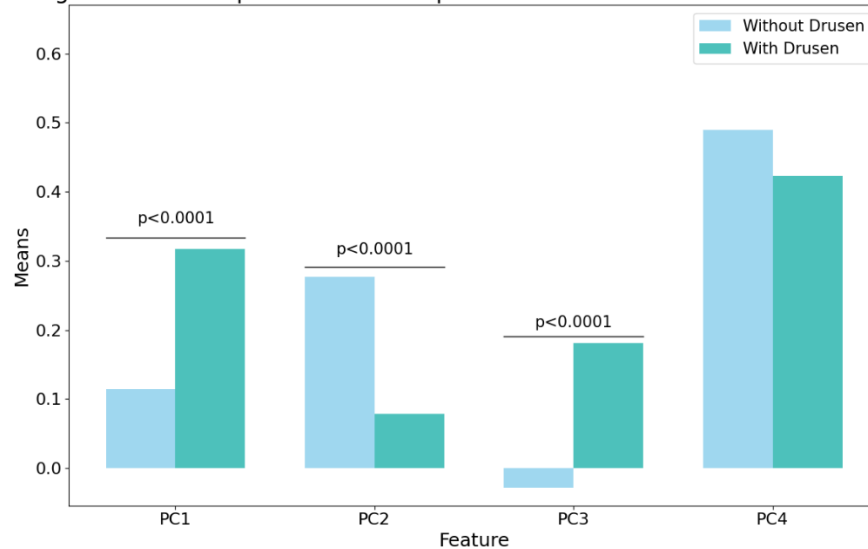
### Spectra Extraction



We applied robust-NMF to an HSI from a patient without drusen lesions and a patient with drusen lesions as seen in Figure 11. The spectra extracted from the HSI through robust-NMF appear visually similar to the spectra extracted in Figure 5 found in Mohammed et al. for healthy and dry AMD patients.<sup>14</sup> This indicates that the spectra extracted by applying the robust-NMF package could be used as ground truth for comparison with the spectra extracted from the EADNMF package. In addition, visually there appears to be a distinction between the spectra extracted from the two patients. The spectrum in red in the image on the right corresponds to drusen lesions in the eye of the dry AMD patient. We compared the spectra obtained between all patients who do not have drusen lesions and all patients who have drusen lesions based on the average principal component value for the first four principal components, as seen in Figure 12, and found the difference in principal component value to be statistically significant for all components. This indicates that robust-NMF can produce distinct spectra that allow us to differentiate between an eye with drusen and an eye without drusen.



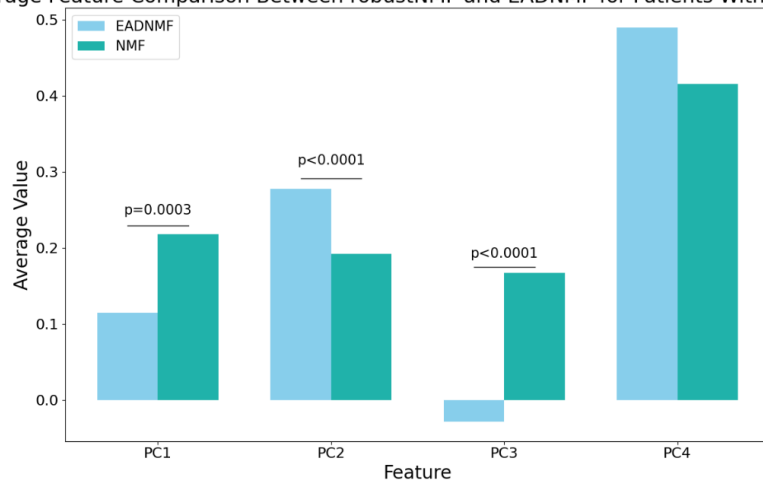
Average Feature Comparison Between patients with and without drusen for EADNMF



**Figure 14.** Comparison of average principal components between spectra extracted from patients with and without drusen lesions using EADNMF.

We applied EADNMF to an HSI from a patient without drusen lesions and a patient with drusen lesions as seen in Figure 13. Visually there appears to be a distinction between spectra extracted from the two patients. The spectrum in green in the image on the right corresponds to drusen lesions in the eye of the dry AMD patient based on spectra extracted in Figure 5 by Mohammed et al. for healthy and dry AMD patients.<sup>14</sup> We compared the spectra obtained between all patients who do not have drusen lesions and all patients who have drusen lesions based on the average principal component value for the first four principal components, as seen in Figure 14, and found the difference to be statistically significant for the first three principal components. This indicates that EADNMF can produce distinct spectra that allow us to differentiate between an eye with drusen and an eye without drusen.

Average Feature Comparison Between robustNMF and EADNMF for Patients Without Drusen



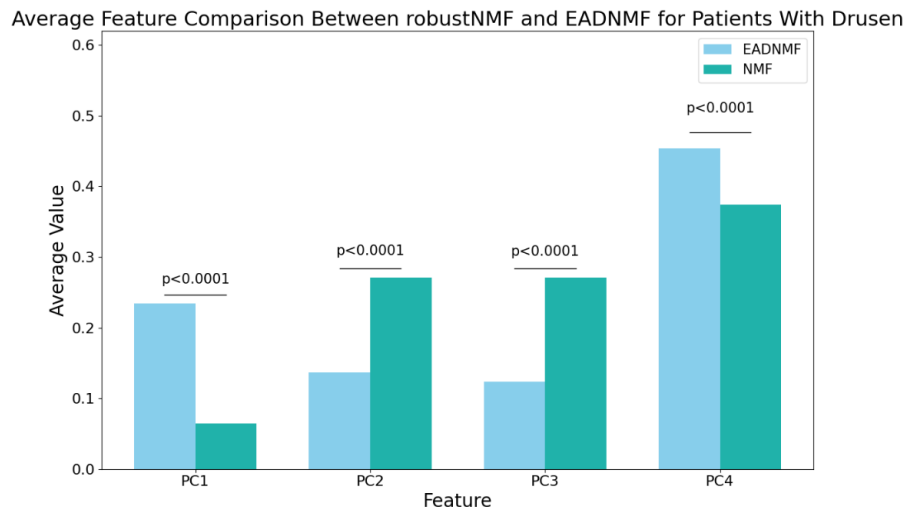


**Figure 15.** Comparison of average principal components between spectra extracted through robust-NMF and EADNMF for patients without (top) and with (bottom) drusen lesions.

Then we wanted to compare the spectra extracted using EADNMF to the spectra extracted using robust-NMF to assess whether deep learning could closely approximate the ground truth. In both patients without drusen lesions and patients with drusen lesions, the difference in average principal component value was statistically significant in the first three principal components between EADNMF and robust-NMF as seen in Figure 15. This indicates that EADNMF extracted spectra did not closely approximate robust-NMF spectra. We hypothesize that this could be due to a small sample size because data for only six patients was available to share as part of an ongoing collaboration with clinicians and scientists at the New York Ear and Eye Infirmary of Mount Sinai. Results for one patient could greatly affect the average principal component value and whether the difference in principal component value was statistically significant. A larger sample size will allow us to draw conclusions about deep learning's ability to extract spectral signatures from HSIs.

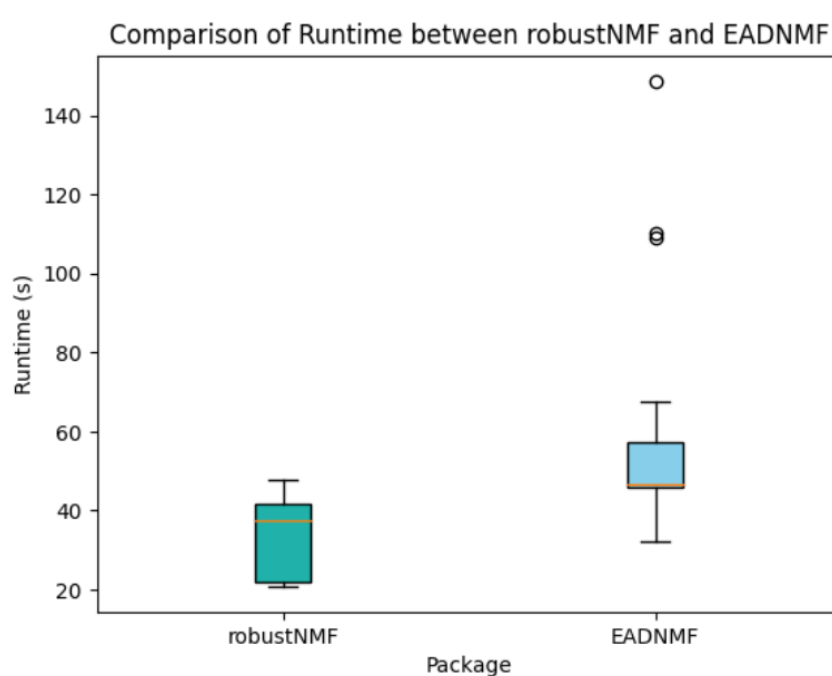


**Figure 16.** Boxplot of run time for robust-NMF and EADNMF to extract spectra from hyperspectral data cubes for all patients.

Finally, we compared run time for both EADNMF and robust-NMF algorithms. As seen in Figure 16, both algorithms had similar median runtimes but we noted that the spread in runtimes was reduced for EADNMF which suggests that EADNMF's runtime and efficiency are not data-dependent. While deep learning could not completely approximate the ground truth, it was able to extract spectral signatures that could be used for the identification of drusen with improved computational efficiency, showcasing its potential for use in the diagnosis of AMD.

## Discussion:

### *Hyperspectral Image Reconstruction*

This paper evaluates three proposed alternatives to the Augmented Lagrangian method of HSI reconstruction—supervised U-Net, self-supervised U-Net, and self-supervised Deep Unfolding network. These models successfully address the main time constraint of iterative methods because neural network models produce results in seconds rather than hours. The self-supervised training setup also avoids overfitting to low quantities of patient data by calculating the loss between the input and output. However, all three tested models failed to achieve a reduction in validation loss and produce useful HSIs. While Figure 7 shows a decrease in validation loss for the supervised U-Net, that model was trained on very low quantities of patient data and therefore, likely produces generalized HSIs that do not capture differences between patient retinas.

Considering the sample wavelengths from HSIs in Figure 9, the significant differences between the iterative method-reconstructed HSIs and model-reconstructed HSIs become apparent. This result is corroborated by the failure to achieve a meaningful decrease in validation loss for the three models after 500 iterations, as shown in Figure 7. Self-supervised learning has previously been utilized to achieve successful HSI reconstruction. Therefore, it is likely that our combination of a self-supervised architecture and the Deep Unfolding model can also achieve success with optimization of the learning rate, compression algorithm, and image pre-processing.

### *Spectra Extraction*

The integration of hyperspectral imaging with advanced machine-learning diagnostic techniques presents a promising trajectory for the efficient and accurate diagnosis of early AMD. Intervention when AMD is in its early stages can help significantly slow the progression of the disease and help preserve the quality of life for affected individuals. The prevalence of AMD globally and the absence of a cure underscores the urgent need for reliable diagnostic tools.

Our application of robust-NMF to hyperspectral data yielded promising results. Visual inspection of the extracted spectra from patients without and with drusen lesions demonstrated distinct differences, aligning with previous studies. The statistically significant differences in the average principal components between patients with and without drusen lesions further underscore the efficacy of robust-NMF in producing spectra capable of distinguishing pathological changes and deterioration in the retina associated with AMD. Similar results are seen with the introduction of deep learning through the EADNMF algorithm. The statistically significant differences in average principal components between patients with and without drusen lesions highlight the potential of EADNMF in providing a computational advantage over current methods. The comparison of the principal components between robust-NMF and EADNMF derived spectra, as depicted in Figure 15, plays a pivotal role in selecting the optimal method for spectral extraction. The analysis indicates that EADNMF-extracted spectra did not closely approximate those obtained through robust-NMF, suggesting that

deep learning may introduce variability that requires further investigation. More data is needed for further analysis to confirm why the EADNMF spectra did not closely approximate the robust-NMF spectra and identify which algorithm is better suited for distinguishing drusens.

The run-time boxplots in Figure 16 provide insights into the computational efficiency of both robust-NMF and EADNMF algorithms. Efficient algorithms are essential for practically implementing diagnostic tools in clinical settings. By comparing run times, we can assess the feasibility and scalability of each algorithm, influencing decisions regarding their integration into diagnostic workflows. The spread of the EADNMF runtimes indicates that it is less data-dependent, making it more scalable and better suited for real-time processing.

The application of deep learning enhances the reconstruction of hyperspectral data and the extraction of spectral signatures associated with AMD. Despite challenges in adapting NMF algorithms to in-vivo data, our ongoing efforts to modify algorithms and account for complexities in living tissues hold promise for more accurate and reliable results. The insights from the representative spectra in Figure 11 can be used for further downstream analysis to optimize and provide crucial insights for diagnostic methodology.

The limitations of our study, including the small sample size and variability introduced by deep learning, emphasize the need for further research. Expanding the dataset will allow for a more comprehensive evaluation of deep learning's spectral extraction capabilities. Additionally, exploring the impact of variations in image acquisition parameters and refining the deep learning model architecture could contribute to improving the accuracy and consistency of spectral extraction.

## References

1. O. Rastoin, G. Pagès, and M. Dufies, "Experimental Models in Neovascular Age Related Macular Degeneration," *International Journal of Molecular Sciences*, vol. 21, no. 13, Jun. 2020, doi: <https://doi.org/10.3390/ijms21134627>.
2. "Amsler Grid Eye Test: A Key Way To Monitor Vision Changes," *Cleveland Clinic*. <https://my.clevelandclinic.org/health/diagnostics/amsler-grid-eye-test>
3. G. Fujimoto, C. Pitris, S. A. Boppart, and M. E. Brezinski, "Optical Coherence Tomography: An Emerging Technology for Biomedical Imaging and Optical Biopsy," *Neoplasia*, vol. 2, no. 1–2, pp. 9–25, Jan. 2000, doi: <https://doi.org/10.1038/sj.neo.7900071>.
4. N. Panwar *et al.*, "Fundus Photography in the 21st Century—A Review of Recent Technological Advances and Their Implications for Worldwide Healthcare," *Telemedicine and e-Health*, vol. 22, no. 3, pp. 198–208, Mar. 2016, doi: <https://doi.org/10.1089/tmj.2015.0068>.
5. S. Lemmens *et al.*, "Hyperspectral Imaging and the Retina: Worth the Wave?," *Translational Vision Science & Technology*, vol. 9, no. 9, pp. 9–9, Aug. 2020, doi: <https://doi.org/10.1167/tvst.9.9.9>.
6. I. García-Sánchez, Ó. Fresnedo, J. P. González-Coma, and L. Castedo, "Coded Aperture Hyperspectral Image Reconstruction," *Sensors*, vol. 21, no. 19, p. 6551, Jan. 2021, doi: <https://doi.org/10.3390/s21196551>.
7. R. Zhao, C. Yang, R. T. Smith, and L. Gao, "Coded aperture snapshot spectral imaging fundus camera," *Scientific Reports*, vol. 13, no. 1, p. 12007, Jul. 2023, doi: <https://doi.org/10.1038/s41598-023-39117-2>.
8. M. Kim *et al.*, "Deep Learning in Medical Imaging," *Neurospine*, vol. 16, no. 4, pp. 657–668, Dec. 2019, doi: <https://doi.org/10.14245/ns.1938396.198>.
9. Li, W. Song, L. Fang, Y. Chen, P. Ghamisi, and J. A. Benediktsson, "Deep Learning for Hyperspectral Image Classification: An Overview," *IEEE Transactions on Geoscience and Remote Sensing*, vol. 57, no. 9, pp. 6690–6709, Sep. 2019, doi: <https://doi.org/10.1109/TGRS.2019.2907932>.
10. C. Juntunen, I. M. Woller, and Y. Sung, "Hyperspectral Three-Dimensional Fluorescence Imaging Using Snapshot Optical Tomography," *Sensors*, vol. 21, no. 11, p. 3652, May 2021, doi: <https://doi.org/10.3390/s21113652>.
11. R. Huang, X. Li, and L. Zhao, "Spectral-Spatial Robust Nonnegative Matrix Factorization for Hyperspectral Unmixing," pp. 453–481, Nov. 2022, doi: <https://doi.org/10.1002/9781119687788.ch16>.
12. N. Dey *et al.*, "Tensor decomposition of hyperspectral images to study autofluorescence in age-related macular degeneration," vol. 56, pp. 96–109, Aug. 2019, doi: <https://doi.org/10.1016/j.media.2019.05.009>.
13. Y. Tong, T. Ach, C. A. Curcio, and R. T. Smith, "Hyperspectral autofluorescence characterization of drusen and sub-RPE deposits in age-related macular degeneration," *Annals of Eye Science*, vol. 6, pp. 4–4, Mar. 2021, doi: <https://doi.org/10.21037/aes-20-12>.
14. Mohammed, T., et al., "Ex Vivo Hyperspectral Autofluorescence Imaging and Localization of Fluorophores in Human Eyes with Age-Related Macular Degeneration," *Vision*, vol. 2, no. 4, 2018, <https://doi.org/10.3390/vision2040038>
15. Dey, N., et al., "Robust-NMF", Github Repository, September 2019, <https://github.com/neel-dey/robust-nmf>
16. Seyed, S., "EADNMF", Github Repository, December 2022, <https://github.com/amjadseyedi/EADNMF/tree/master>
17. Seyed, S., et al., "Elastic adversarial deep nonnegative matrix factorization for matrix completion," *Information Sciences*, vol. 621, pp. 562–579, April 2023, <https://doi.org/10.1016/j.ins.2022.11.120>
18. Ronneberger, O., Fischer, P., Brox, T. (2015). U-Net: Convolutional Networks for Biomedical Image Segmentation. In: Navab, N., Hornegger, J., Wells, W., Frangi, A. (eds) Medical Image Computing and Computer-Assisted Intervention – MICCAI 2015. MICCAI 2015. Lecture Notes in Computer Science(), vol 9351. Springer, Cham. [https://doi.org/10.1007/978-3-319-24574-4\\_28](https://doi.org/10.1007/978-3-319-24574-4_28)